

See discussions, stats, and author profiles for this publication at: <https://www.researchgate.net/publication/44887104>

Ion transport in nanofluidic funnels. ACS Nano 4:3897-3902

ARTICLE in ACS NANO · JULY 2010

Impact Factor: 12.88 · DOI: 10.1021/nn100692z · Source: PubMed

CITATIONS

48

READS

44

4 AUTHORS, INCLUDING:



John Perry

University of North Carolina at Chapel Hill

11 PUBLICATIONS 245 CITATIONS

SEE PROFILE



Zachary Harms

Indiana University Bloomington

10 PUBLICATIONS 110 CITATIONS

SEE PROFILE

Ion Transport in Nanofluidic Funnels

John M. Perry, Kaimeng Zhou, Zachary D. Harms, and Stephen C. Jacobson*

Department of Chemistry, Indiana University, Bloomington, Indiana 47405-7102

Ion transport, sensing, and separations with nanopores and nanochannels have received substantial attention because of the unique transport properties they exhibit¹ and their potential applications.² As one example, nanofluidic pores and channels with asymmetric features are able to rectify ion current. For ion rectification to occur, one lateral dimension of the channel is typically on the nanoscale and a geometric or surface charge asymmetry exists along the axis of ion current flow.³ Ion current rectification was first reported in a quartz nanopipette,⁴ and since that report, rectification has been observed in track-etched polymer membranes,^{5,6} silicon-based nanochannels,⁷ and poly(lysine)-coated quartz nanopipettes.⁸ Ion pumping up a concentration gradient shows a pH dependence of rectification,⁹ and internal surface charge of the nanopore is a critical parameter in controlling rectification.¹⁰ Nanochannels have also exhibited ion permselectivity,¹¹ ion enrichment and depletion,^{12–14} and enhanced channel conductance.¹⁵ Track-etched nanopores are well-studied because a simple and reliable fabrication method for conical pores is available,⁵ and the pore size, taper angle, and geometry in conical nanopores can be controlled to some extent by application of a potential during etching¹⁶ and addition of surfactants¹⁷ and organic solvents¹⁸ to the etchant solution. Unfortunately, the exact dimensions and geometries of track-etched pores are not known in many experiments.

Standard micro- and nanofabrication techniques, however, can create features with a wide range of well-defined geometries and dimensions and have been used to produce a number of nanofluidic devices.¹⁹ For example, nanofluidic devices

ABSTRACT We report fabrication of nanofluidic channels with asymmetric features (*e.g.*, funnels) that were cast in high modulus poly(dimethylsiloxane) and had well-defined geometries and dimensions. Masters used to cast the funnels were written in the negative tone resist SU-8 by electron beam lithography. Replicated funnels had taper angles of 5, 10, and 20° and were 80 nm wide at the tip, 1 μm wide at the base, and 120 nm deep. The planar format permitted easy coupling of the funnels to microfluidic channels and simultaneous electrical and optical characterization of ion transport. All three designs rectified ion current, and the 5° funnel exhibited the highest rectification ratio. Fluorescence measurements at the funnel base showed that an anionic probe was enriched and depleted in the high and low conductance states, respectively.

KEYWORDS: nanofluidics · nanochannel · nanofunnel · ion current rectification · electron beam lithography · high modulus poly(dimethylsiloxane)

have been fabricated by photolithography and wet etching,²⁰ electron beam (e-beam) drilling,²¹ focused ion beam milling,²² femtosecond laser machining,²³ micromolding techniques,²⁴ nanoimprint lithography,²⁵ and grayscale lithography.²⁶ Electron and ion beam techniques are of particular interest because these techniques are able to form features in which one or two dimensions (*i.e.*, width and depth) are confined to the nanoscale. In addition, nanofluidic channels coupled to microfluidic channels provide a platform for studying the ion transport behavior and conducting analytical assays.² Integration of many of these nanochannel elements with microchannels is straightforward, and when a planar format is used, multiple nanochannels can be easily coupled together.²⁷

In our work, we chose to use e-beam lithography to create molds for in-plane nanochannels with asymmetric features, such as funnels, where both width and depth were confined to the nanoscale. E-beam lithography permits features as small as 30 nm wide to be written in the negative tone resist SU-8,^{28,29} and we used e-beam lithography to define the

*Address correspondence to jacobson@indiana.edu.

Received for review April 6, 2010 and accepted June 16, 2010.

Published online June 30, 2010. 10.1021/nn100692z

© 2010 American Chemical Society

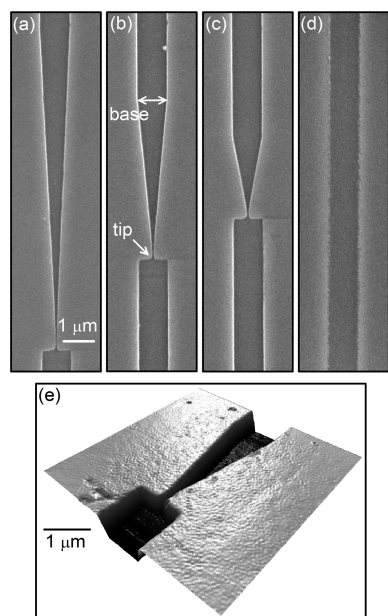


Figure 1. Scanning electron microscope (SEM) images of nanofunnels with (a) 5°, (b) 10°, and (c) 20° taper angles and (d) a straight nanochannel, and (e) atomic force microscope (AFM) image of the 20° funnel. These structures were cast in high modulus poly(dimethylsiloxane) on an SU-8 master formed by electron beam lithography. See Table 1 for tip dimensions of the funnels.

funnel width and the resist thickness to set the channel depth. E-beam written SU-8 masters were then used to cast funnels with taper angles of 5, 10, and 20° and a straight channel in high modulus poly(dimethylsiloxane) (h-PDMS),^{30,31} which provides good replication fidelity of nanoscale features. After fabrication, current–voltage (*I*/*V*) behavior was examined with buffer concentrations from 1 to 510 mM, and the ion current rectified for all three funnel designs. The rectification ratio, which is the absolute value of the ratio of currents measured at potentials of equal magnitude but opposite sign, was highest for the 5° funnel and at the lowest buffer concentrations tested. We also used fluorescence microscopy to track ion transport through the funnels and confirmed ion enrichment and depletion at the funnel base.

RESULTS AND DISCUSSION

Funnel Geometries and Dimensions. We fabricated nanoscale funnels by casting h-PDMS onto an SU-8 master written by e-beam lithography. The thin layer of h-PDMS was supported by forming a composite replica³¹ with poly(dimethylsiloxane) (PDMS). We used a scanning electron microscope (SEM) to determine the channel widths of the master and replicas and an atomic force microscope (AFM) to measure the channel heights/depths of the master and replicas. Four replicas, each with the four channel designs, were cast from the master. Figure 1 shows SEM and AFM images of the h-PDMS replicas, and the master and replica dimensions are listed in Table 1. The funnel replicas were

TABLE 1. Tip Dimensions for 5, 10, and 20° Funnels

	width (nm) ^a		height and depth (nm) ^b	
	master	replica	master ^c	replica ^d
5° funnel	75 ± 2	77 ± 5	116 ± 4	122 ± 4
10° funnel	80 ± 5	77 ± 8	128 ± 2	121 ± 3
20° funnel	75 ± 3	81 ± 4	127 ± 2	120 ± 7

^aMeasured by scanning electron microscope; *n* = 3 for each funnel design. ^bMeasured by atomic force microscope. ^c*n* = 10 for each funnel design. ^d*n* = 20 for each funnel design; five measurements on four 5° funnels, 10° funnels, and 20° funnels.

80 nm wide and 120 nm deep at the tip and 1.06 μm wide and 120 nm deep at the base, and the funnel lengths were 11.5, 5.7, and 2.9 μm for the 5, 10, and 20° funnels, respectively. The straight channels were 1.06 μm wide and 120 nm deep. The h-PDMS replicas were 2% wider and 2% shallower than the SU-8 master, indicating accurate reproduction of the master by the replicas. For electrical and optical characterization, the h-PDMS replicas were reversibly sealed to a glass substrate with two microchannels, so that the nanochannel bridged the microchannels. Figure 2a shows a bright-field image of a device with the 5° funnel connecting two microchannels. Straight nanochannels (~40 μm long, 1 μm wide, and 120 nm deep) connected the tip and base of each funnel to the two microchannels, which were spaced 85 μm apart. The 5, 10, and 20° funnels contributed 13.5, 6.7, and 3.4%, respectively, to the total nanochannel length between the two microchannels and had identical fluid connections at the tip and base.

Ion Transport in Funnels. Current–voltage (*I*/*V*) curves were collected for each nanochannel. In all experiments, the working electrode was at the base of the funnel and the counter electrode at the tip of the funnel. With the counter electrode held at 0 V, potentials at the working electrode were stepped at 0.1 V/step for 0.5 s/step (0.2 V/s) from −1 to 1 V in triplicate and then

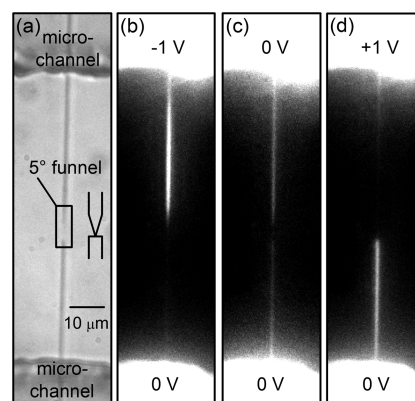


Figure 2. (a) Bright-field image of the 5° funnel bridging two microchannels, and fluorescence images of fluorescein transported through the 5° funnel with 0 V applied to the tip and (b) −1 V applied to the base, (c) 0 V applied to the base, and (d) +1 V applied to the base. In part (a), the inset is a schematic of the funnel with the tip pointing down, and the rectangle highlights the position of the 5° funnel along the 85 μm long nanochannel. Buffer was 1 mM phosphate.

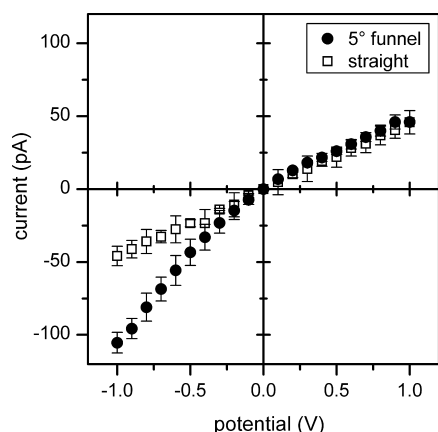


Figure 3. Current–voltage (*IV*) curves for four 5° funnels and three straight channels filled with 1 mM phosphate buffer. The potential applied to the base was swept at 0.2 V/s with 0 V applied to the tip. Error bars are $\pm \sigma$ and were calculated from six *IV* curves on four 5° funnels ($n = 24$) and from six *IV* curves on three straight channels ($n = 18$).

at 0.2 V/s from +1 to −1 V in triplicate. Due to the high resistance of the nanochannels compared to the microchannels, 98% of the potential was dropped across the nanochannel, and consequently, the potentials are reported as the potential applied to the reservoirs. In Figure 3, *IV* curves for the 5° funnel and straight channel filled with 1 mM phosphate buffer are compared. As seen in the figure, the straight channel exhibited ohmic behavior, while the 5° funnel rectified ion current. The *IV* curve shows that when the potential applied to the working electrode at the funnel base was positive, the counterions (cations) moved from base to tip, and the current was similar to the straight channel. Counterion flow from base to tip is referred to as the low conductance (*G*) state. On the other hand, when the potential applied to the working electrode was negative, the counterions migrated from tip to base, and the current was two times higher than the straight channel. Counterion flow from tip to base is referred to as the high conductance (*G*) state. A straight channel with a smaller cross section (e.g., 100 nm wide and 120 nm deep) produced *IV* curves similar to the straight channel in Figure 3, except the channel resistance was higher, and the slope of the *IV* curve was shallower.

Figure 4 shows variation of the rectification ratios for the 5, 10, and 20° funnels and straight channel with buffer concentration. From the *IV* curves, the rectification ratio was calculated and is the absolute value of the current measured at −0.9 V divided by the current measured at +0.9 V. All three funnel designs exhibited rectification, and as expected, the rectification ratio increased with decreasing ionic strength. Interestingly, the rectification ratio decreased with increasing taper angle, with the 5° funnel showing the highest rectification ratio (2.0) at the lowest buffer concentration tested (1 mM). Only a few experimental studies have been published showing rectification in an isolated nanochannel with a diameter ≥ 50 nm, and each of these stud-

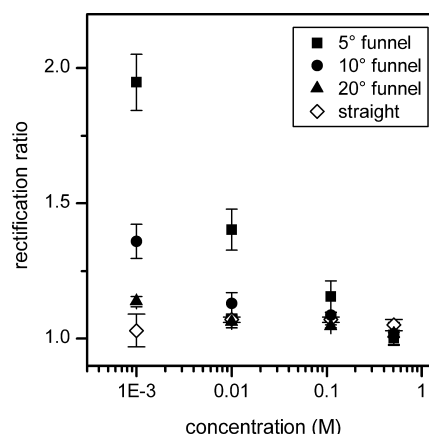


Figure 4. Variation of the rectification ratio with phosphate buffer concentration for four 5° funnels and three 10° funnels, 20° funnels, and straight channels. The rectification ratio is the absolute value of current measured at −0.9 V divided by the current measured at +0.9 V. Error bars are $\pm \sigma$ and were calculated from six *IV* curves on four 5° funnels ($n = 24$) and from six *IV* curves on three 10° funnels, 20° funnels, and straight channels ($n = 18$ each).

ies examined only a single pore diameter.^{8,32,33} More recently, large conical nanopores (e.g., > 300 nm tip diameter) exhibited diode-like *IV* behavior that rivals much smaller nanopores.³⁴

How the conductivity of the 5° funnel in the high and low conductance states varied with buffer concentration was extracted from the *IV* curves and is depicted in Figure 5. These data are compared to the conductivities in the straight channel and bulk buffer. As expected, the conductivities were similar at high buffer concentrations but diverged as the buffer concentration decreased. Consistent with Figures 3 and 4, the 5° funnel had the highest conductivities when in the high conductance state. The 5° funnel in the low conductance state and straight channel had similar conductivities and were higher than the bulk buffer. The straight channel with a higher conductivity than bulk buffer was

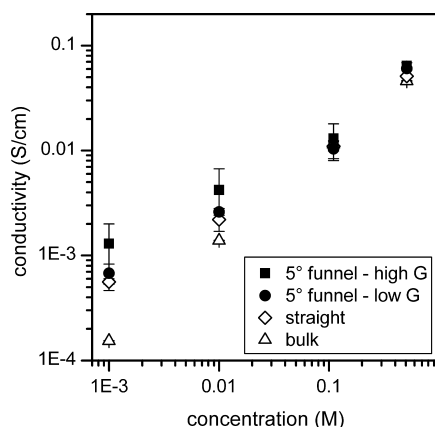


Figure 5. Variation of the conductivity with buffer concentration for four 5° funnels in the low and high conductance (*G*) states, three straight channels, and bulk buffer. Error bars are $\pm \sigma$ and were calculated from six *IV* curves on four 5° funnels ($n = 24$), from six *IV* curves on three straight channels ($n = 18$), and from six measurements of the bulk buffer conductivity ($n = 6$).

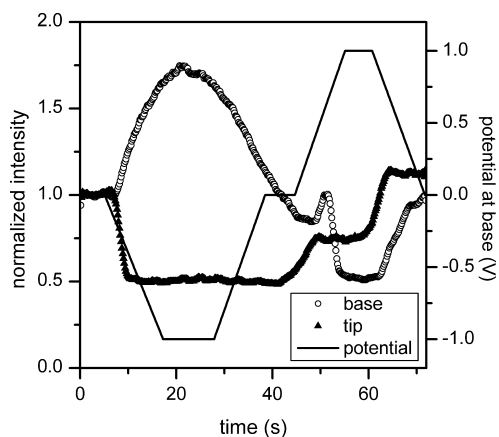


Figure 6. Variation of the normalized fluorescence intensity with time at the base and tip of the 5° funnel. The potential applied to the base is plotted with time, and the potential applied to the tip was 0 V. Intensity measurements were normalized to the initial value, and buffer was 1 mM phosphate.

consistent with previous reports.¹⁵ The 10 and 20° funnels exhibited conductivity behavior similar to that of the 5° funnel, except the differences between the high and low conductance states were smaller.

Fluorescence Imaging. In addition to the electrical characterization, ion transport through the nanochannels was monitored by fluorescence. Figure 2 shows fluorescence images of fluorescein in the 5° funnel. With -1 V applied to the funnel base, fluorescein accumulated above the funnel on the base side, and with $+1$ V applied to the funnel base, fluorescein accumulated below the funnel tip. With no potential difference between the funnel base and tip, fluorescein uniformly filled the nanochannel. When a constant potential difference was applied between the funnel base and tip, the fluorescence intensity quickly reached a steady state in ~ 1 s, and the intensity did not continue to increase. Similarly, the current reached a steady state value in the same time period. These results suggested that asymmetry in the nanochannels resulted in localized enrichment and depletion, but diffusive transport from the microchannel was sufficient to maintain a supply of ions to the nanochannels.

The fluorescence intensity was also monitored during potential sweeps similar to the *IV* curves in Figure 3. Figure 6 compares the fluorescence intensity at the funnel base and tip for the 5° funnel. In this experiment, the potential applied to the base is depicted in Figure 6 and was stepped at the same rate (e.g., 0.2 V/s) between -1 and $+1$ V. A video that shows how the fluorescence varied with applied potential is included in the Supporting Information. Intensity measurements were made by integrating the fluorescence signal from a $1.2\ \mu\text{m} \times 0.5\ \mu\text{m}$ area at the funnel base and tip and normalizing to the initial value. When the potential at the base was negative relative to the tip (high *G*), the fluorescence intensity at the base was higher than the fluorescence intensity when no potential difference was

applied (initial value), and when the potential at the base was positive relative to the tip, the fluorescence intensity was lower (low *G*). The fluorescence at the funnel tip showed the opposite trend when compared to the fluorescence at the base. If electrical neutrality is assumed, the fluorescein concentration mimicked the counterion concentration and reflected the ion concentration at the funnel base and tip during the potential sweep.

These fluorescence data can also be used to generate a rectification ratio by taking the fluorescence intensity when the potential at the base was negative and dividing by the fluorescence intensity when the potential at the tip was positive. As seen in Figure 6, the normalized fluorescence intensity at the base of the 5° funnel was high when the potential at the base was negative and low when the potential was positive. For comparison, the straight channel showed no change in relative intensity during the potential sweeps. The rectification ratios derived from fluorescence measurements showed the same trend as the rectification ratios in Figure 4 extracted from *IV* curves.

Rectification in Funnels. The high conductance state can be attributed to an increase in ion concentration within the funnel. This effect is predicted by calculations based on a membrane model with small diameter pores³⁵ and numerical analysis of the Poisson–Nernst–Planck equations.^{36–40} These models suggest that rectification arises from a difference between the transference numbers for the counterions at the funnel tip and base. At the funnel tip, a larger fraction of the current was carried by the surface charge than at the funnel base. When counterion transport was from tip to base (high *G*), the counterions moved from a region of higher transference number at the funnel tip to a region of lower transference number region at the funnel base. Counterions accumulated in the funnel, yielding higher currents through the funnel and higher fluorescence at the funnel base. When the polarity of the applied potential was reversed and the counterions traveled from base to tip, the counterions moved from a region of lower transference number to a region of higher transference number, resulting in lower current through the funnel and lower fluorescence at the funnel base. The taper angle influences where and to what extent enrichment and depletion occur,³⁷ but the impact of taper angle on the rectification ratio is not known. The conductivity of the 5° funnel in the high conductance state with the 1 mM phosphate buffer was 25 and 47% higher than in the 10 and 20° funnels, respectively. The 5° funnel had two and four times more total surface area than the 10 and 20° funnels, respectively (see Figure 1), but the surface-to-volume ratios for all three designs were similar. Enrichment and depletion of ions in the funnels led to rectification, and the length and total surface area of the 5° funnel contributed to efficient

formation of these regions, where higher rectification was observed.

CONCLUSION

E-beam lithography provided greater control of the lateral dimensions of the nanoscale features (e.g., tip and base dimensions of the funnels) and allowed the taper angle of the funnels to be varied easily. Channels and funnels cast in h-PDMS reproduced the e-beam written masters within 2% RSD. The planar format also allowed direct visualization of the rectification process by tracking the concentration and depletion of a fluorescent probe. The combination of electrical and optical

characterization demonstrated that the funnel geometry (e.g., taper angle, length, and surface area) contributed to the rectification process. Moreover, larger rectification ratios are observed in nanochannels with smaller cross sections. SU-8 masters of nanochannels with feature sizes as small as 30 nm can be created on e-beam instruments with higher accelerating potentials^{28,29} or by e-beam induced etching⁴¹ of the masters after e-beam lithography (unpublished data). In addition, the planar format will permit fabrication of multiple nanofluidic features in series or parallel to better understand and take advantage of electrokinetic processes at the nanoscale.

METHODS

Funnel Fabrication. Nanoscale funnels were fabricated by casting a high modulus poly(dimethylsiloxane) (h-PDMS) onto a master written by e-beam lithography. Glass substrates (24 mm × 30 mm) were cleaned with methanol and spin-coated with AP300 (Silicon Resources) to promote adhesion of the negative tone resist SU-8 2010 (MicroChem Corp.). The SU-8 resist was diluted 1:10 in cyclopentanone and spin-coated at 9000 rpm onto the glass substrates for 30 s to form a 120 nm layer. The SU-8 film was prebaked at 60 °C for 1 min and at 90 °C for 3 min. A scanning electron microscope (SEM; Quanta 600F, FEI Company) equipped with Nanometer Pattern Generation System (JC Nabity Lithography Systems) was used to write nanochannel patterns into the SU-8 layer. To ensure uniform feature heights, the master contained all four nanochannel designs: a 5° funnel, 10° funnel, 20° funnel, and straight channel. After e-beam exposure, the SU-8 was postbaked similar to the prebake and was developed in a Nano PG Developer (MicroChem Corp.) for 1 min.

The h-PDMS polymer was formed by choosing an appropriate vinyl and hydrosilane copolymer ratio that provides a high cross-linking density.^{30,31} A mixture of 3.4 g of vinyl PDMS prepolymer (VDT-731, Gelest Corp.), 1.0 g of a hydrosilane PDMS prepolymer (HMS-301, Gelest Corp.), 20 μ L of a platinum catalyst (platinum carbonyl cyclovinylmethylsiloxane, SIP6829.2, Gelest Corp.), and 0.1 g of modulator (1,3,5,7-tetravinyl-1,3,5,7-tetramethylcyclotetrasiloxane, SIT7900.0, Gelest Corp.) was degassed in vacuum. The h-PDMS was spin-coated onto the SU-8 master at 9000 rpm for 30 s to create a \sim 10 μ m thick layer. To ensure proper replication of the master geometry, the sample was left at room temperature for 1 h prior to curing to allow the h-PDMS to conform to the master and to allow for the remaining solvent to evaporate.⁴² The h-PDMS was then cured in an oven at 60 °C for 30 min. To support the thin layer of h-PDMS, a 3 mm thick layer of PDMS in a 10:1 mixture (Sylgard 184, Dow Corning Corp.) was applied on top of the h-PDMS. The composite mold was then cured at 60 °C for 1 h. We used the same SEM to determine the channel widths of the master and replicas and an AFM (MFP3d, Asylum Research) to measure the channel heights and depths of the master and replicas, respectively.

Glass substrates with two V-shaped microchannels were fabricated as previously described⁴³ and used to provide fluidic and electrical access to the nanochannels. The microchannels were 10 μ m deep, 70 μ m wide at the top, and 1 cm long. The h-PDMS replica with the nanochannel was reversibly bonded to the glass substrate, so that the nanochannel bridged the two microchannels. For bonding, the h-PDMS substrate with the nanochannel and the glass substrate with the microchannels were rinsed with methanol, dried in a stream of nitrogen, and brought into contact with each other, forming a reversible seal between the two substrates. Figure 2a shows a bright-field image of a device with the 5° funnel connecting two microchannels. The gap between the two microchannels was 85 μ m, and the nanofunnel was approximately centered between the microchannels.

Current Measurements. A picoammeter/voltage source (6487 Keithley Instruments, Inc.) was used to collect current–voltage (*I/V*) curves from four 5° funnels and three 10° funnels, 20° funnels, and straight channels. Silver–silver chloride wire electrodes were used to make electrical connections to the buffer reservoirs, which were positioned at the ends of the V-shaped microchannels. The *I/V* curves were adjusted to zero current at zero volts to remove small offsets experienced between runs. The currents at \pm 0.9 V were used for calculating the rectification ratio because the *I/V* measurements periodically yielded an erroneous point at the start of the scan. The four potassium phosphate buffers tested were (1) 1 mM potassium phosphate, (2) 10 mM potassium phosphate, (3) 10 mM potassium phosphate with 100 mM NaCl, and (4) 10 mM potassium phosphate with 500 mM NaCl.

Optical Microscopy. Images of accumulation and depletion of an anionic probe, disodium fluorescein (100 μ M in buffer, Sigma-Aldrich Co.), were taken with an inverted optical microscope (TE2000-E, Nikon, Inc.) equipped with 40 \times and 60 \times objectives, an HQ FITC filter cube (Chroma Technology Corp.), Intensilight source, and CCD camera (Cascade 512B, Photometrics). The images of the fluorescein were captured with exposure times of 50 ms or 1 s and analyzed with IPLab software (BD Biosciences).

Acknowledgment. This work was supported in part by NSF CHE-0750295, NSF CHE-0832651, and the Indiana METACyt Initiative of Indiana University, funded in part through a major grant from the Lilly Endowment, Inc.

Supporting Information Available: Video of fluorescein transported through the 5° funnel (see Figure 2 for details). This material is available free of charge via the Internet at <http://pubs.acs.org>.

REFERENCES AND NOTES

- Schoch, R. B.; Han, J.; Renaud, P. Transport Phenomena in Nanofluidics. *Rev. Mod. Phys.* **2008**, *80*, 839–883.
- Kovarik, M. L.; Jacobson, S. C. Nanofluidics in Lab-on-a-Chip Devices. *Anal. Chem.* **2009**, *81*, 7133–7140.
- Siwy, Z. S. Ion-Current Rectification in Nanopores and Nanotubes with Broken Symmetry. *Adv. Funct. Mater.* **2006**, *16*, 735–746.
- Wei, C.; Bard, A. J.; Feldberg, S. W. Current Rectification at Quartz Nanopipet Electrodes. *Anal. Chem.* **1997**, *69*, 4627–4633.
- Apel, P. Y.; Korchev, Y. E.; Siwy, Z.; Spohr, R.; Yoshida, M. Diode-like Single-Ion Track Membrane Prepared by Electro-Stopping. *Nucl. Instrum. Methods Phys. Res., Sect. B* **2001**, *184*, 337–346.
- Siwy, Z.; Fulinski, A. Fabrication of a Synthetic Nanopore Ion Pump. *Phys. Rev. Lett.* **2002**, *89*, 198103.
- Karnik, R.; Duan, C.; Castelino, K.; Daiguji, H.; Majumdar, A. Rectification of Ionic Current in a Nanofluidic Diode. *Nano Lett.* **2007**, *7*, 547–551.
- Umehara, S.; Pourmand, N.; Webb, C. D.; Davis, R. W.;

- Yasuda, K.; Karhanek, M. Current Rectification with Poly-L-Lysine-Coated Quartz Nanopipettes. *Nano Lett.* **2006**, *6*, 2486–2492.
9. Siwy, Z.; Apel, P.; Dobrev, D.; Neumann, R.; Spohr, R.; Trautmann, C.; Voss, K. Ion Transport through Asymmetric Nanopores Prepared by Ion Track Etching. *Nucl. Instrum. Methods Phys. Res., Sect. B* **2003**, *208*, 143–148.
 10. Siwy, Z.; Heins, E.; Harrell, C. C.; Kohli, P.; Martin, C. R. Conical-Nanotube Ion-Current Rectifiers: The Role of Surface Charge. *J. Am. Chem. Soc.* **2004**, *126*, 10850–10851.
 11. Siwy, Z.; Kosinska, I. D.; Fulinski, A.; Martin, C. R. Asymmetric Diffusion through Synthetic Nanopores. *Phys. Rev. Lett.* **2005**, *94*, 048102.
 12. Pu, Q.; Yun, J.; Temkin, H.; Liu, S. Ion-Enrichment and Ion-Depletion Effect of Nanochannel Structures. *Nano Lett.* **2004**, *4*, 1099–1103.
 13. Wang, Y.-C.; Stevens, A. L.; Han, J. Million-Fold Preconcentration of Proteins and Peptides by Nanofluidic Filter. *Anal. Chem.* **2005**, *77*, 4293–4299.
 14. Zhou, K.; Kovarik, M. L.; Jacobson, S. C. Surface-Charge Induced Ion Depletion and Sample Stacking near Single Nanopores in Microfluidic Devices. *J. Am. Chem. Soc.* **2008**, *130*, 8614–8616.
 15. Stein, D.; Kruithof, M.; Dekker, C. Surface-Charge-Governed Ion Transport in Nanofluidic Channels. *Phys. Rev. Lett.* **2004**, *93*, 035901.
 16. Harrell, C. C.; Siwy, Z. S.; Martin, C. R. Conical Nanopore Membranes: Controlling the Nanopore Shape. *Small* **2006**, *2*, 194–198.
 17. Apel, P. Y.; Blonskaya, I. V.; Orelovitch, O. L.; Root, D.; Vutsadakis, V.; Dmitriev, S. N. Effect of Nanosized Surfactant Molecules on the Etching of Ion Tracks: New Degrees of Freedom in Design of Pore Shape. *Nucl. Instrum. Methods Phys. Res., Sect. B* **2003**, *209*, 329–334.
 18. Guo, W.; Xue, J.; Wang, L.; Wang, Y. Controllable Etching of Heavy Ion Tracks with Organic Solvent Addition in Etchant. *Nucl. Instrum. Methods Phys. Res., Sect. B* **2008**, *266*, 3095–3099.
 19. Mijatovic, D.; Eijkel, J. C. T.; van den Berg, A. Technologies for Nanofluidic Systems: Top-Down vs Bottom-Up—A Review. *Lab Chip* **2005**, *5*, 492–500.
 20. Han, J.; Craighead, H. G. Separation of Long DNA Molecules in a Microfabricated Entropic Trap Array. *Science* **2000**, *288*, 1026–1029.
 21. Storm, A. J.; Chen, J. H.; Ling, X. S.; Zandbergen, H. W.; Dekker, C. Fabrication of Solid-State Nanopores with Single-Nanometre Precision. *Nat. Mater.* **2003**, *2*, 537–540.
 22. Li, J.; Stein, D.; McMullan, C.; Branton, D.; Aziz, M. J.; Golovchenko, J. A. Ion-Beam Sculpting at Nanometre Length Scales. *Nature* **2001**, *412*, 166–169.
 23. Uram, J. D.; Ke, K.; Hunt, A. J.; Mayer, M. Label-Free Affinity Assays by Rapid Detection of Immune Complexes in Submicrometer Pores. *Angew. Chem., Int. Ed.* **2006**, *45*, 2281–2285.
 24. Saleh, O. A.; Sohn, L. L. An Artificial Nanopore for Molecular Sensing. *Nano Lett.* **2003**, *3*, 37–38.
 25. Guo, L. J.; Cheng, X.; Chou, C.-F. Fabrication of Size-Controllable Nanofluidic Channels by Nanoimprinting and Its Application for DNA Stretching. *Nano Lett.* **2004**, *4*, 69–73.
 26. Stavis, S. M.; Strychalski, E. A.; Gaitan, M. Nanofluidic Structures with Complex Three-Dimensional Surfaces. *Nanotechnology* **2009**, *20*, 165302.
 27. Fu, J.; Schoch, R. B.; Stevens, A. L.; Tannenbaum, S. R.; Han, J. A Patterned Anisotropic Nanofluidic Sieving Structure for Continuous-Flow Separation of DNA and Proteins. *Nat. Nanotechnol.* **2007**, *2*, 121–128.
 28. Aktary, M.; Jensen, M. O.; Westra, K. L.; Brett, M. J.; Freeman, M. R. High-Resolution Pattern Generation Using the Epoxy Novolak SU-8 2000 Resist by Electron Beam Lithography. *J. Vac. Sci. Technol., B* **2003**, *21*, L5–L7.
 29. Bilenberg, B.; Jacobsen, S.; Schmidt, M. S.; Skjolding, L. H. D.; Shi, P.; Bøggild, P.; Tegenfeldt, J. O.; Kristensen, A. High Resolution 100 kV Electron Beam Lithography in SU-8. *Microelectron. Eng.* **2006**, *83*, 1609–1612.
 30. Schmid, H.; Michel, B. Siloxane Polymers for High-Resolution, High-Accuracy Soft Lithography. *Macromolecules* **2000**, *33*, 3042–3049.
 31. Odom, T. W.; Love, J. C.; Wolfe, D. B.; Paul, K. E.; Whitesides, G. M. Improved Pattern Transfer in Soft Lithography Using Composite Stamps. *Langmuir* **2002**, *18*, 5314–5320.
 32. Wang, J.; Martin, C. R. A New Drug-Sensing Paradigm Based on Ion-Current Rectification in a Conically Shaped Nanopore. *Nanomedicine* **2008**, *3*, 13–20.
 33. Jung, J.-Y.; Joshi, P.; Petrossian, L.; Thornton, T. J.; Posner, J. D. Electromigration Current Rectification in a Cylindrical Nanopore Due to Asymmetric Concentration Polarization. *Anal. Chem.* **2009**, *81*, 3128–3133.
 34. Kovarik, M. L.; Zhou, K.; Jacobson, S. C. Effect of Conical Nanopore Diameter on Ion Current Rectification. *J. Phys. Chem. B* **2009**, *113*, 15960–15966.
 35. Woermann, D. Electrochemical Transport Properties of a Cone-Shaped Nanopore: High and Low Electrical Conductivity States Depending on the Sign of an Applied Electrical Potential Difference. *Phys. Chem. Chem. Phys.* **2003**, *5*, 1853–1858.
 36. Cervera, J.; Schiedt, B.; Neumann, R.; Mafé, S.; Ramírez, P. Ionic Conduction, Rectification, and Selectivity in Single Conical Nanopores. *J. Chem. Phys.* **2006**, *124*, 104706.
 37. Liu, Q.; Wang, Y.; Guo, W.; Ji, H.; Xue, J.; Ouyang, Q. Asymmetric Properties of Ion Transport in a Charged Conical Nanopore. *Phys. Rev. E* **2007**, *75*, 051201.
 38. Wang, X.; Xue, J.; Wang, L.; Guo, W.; Zhang, W.; Wang, Y.; Liu, Q.; Ji, H.; Ouyang, Q. How the Geometric Configuration and the Surface Charge Distribution Influence the Ionic Current Rectification in Nanopores. *J. Phys. D: Appl. Phys.* **2007**, *40*, 7077–7084.
 39. White, H. S.; Bund, A. Ion Current Rectification at Nanopores in Glass Membranes. *Langmuir* **2008**, *24*, 2212–2218.
 40. Ramírez, P.; Apel, P. Y.; Cervera, J.; Mafé, S. Pore Structure and Function of Synthetic Nanopores with Fixed Charges: Tip Shape and Rectification Properties. *Nanotechnology* **2008**, *19*, 315707.
 41. Randolph, S. J.; Fowlkes, J. D.; Rack, P. D. Focused, Nanoscale Electron-Beam-Induced Deposition and Etching. *Crit. Rev. Solid State Mater. Sci.* **2006**, *31*, 55–89.
 42. Kang, H.; Lee, J.; Park, J.; Lee, H. H. An Improved Method of Preparing Composite Poly(dimethylsiloxane) Moulds. *Nanotechnology* **2006**, *17*, 197–200.
 43. Kovarik, M. L.; Jacobson, S. C. Attoliter-Scale Dispensing in Nanofluidic Channels. *Anal. Chem.* **2007**, *79*, 1655–1660.